Chemical Insights into the Formation of Metastable Zinc Cobalt Sulfide Solid-Solution Nanoparticles through Simultaneous Multi-Cation Exchange

Connor R. McCormick,[1] Steven M. Baksa,[2] Joseph M. Veglak,[1] Ismaila Dabo,[2,3,*] and Raymond E. Schaak[1,3,4,*]

[1]*Department of Chemistry,* [2]*Department of Materials Science and Engineering,* [3]*Materials Research Institute, and* [4]*Department of Chemical Engineering, The Pennsylvania State University, University Park, PA 16802, United States.*

ABSTRACT

Nanoparticle materials that consist of a solid solution between two end member compounds often have composition-dependent physical properties. Their synthesis can be challenging as it requires balancing the competing reactivities of many different reagents to favor the formation of a single-phase product rather than a phase-segregated mixture of its end members. Here, we provide chemical insights into the synthesis of wurtzite $Co_xZn_{1-x}S$ nanoparticle spheres, rods, and plates for x = 0.25, 0.50, and 0.75, which represent solid solutions of CoS and ZnS, by simultaneously exchanging the Cu^+ cations in roxbyite copper sulfide for Zn^{2+} and Co^{2+}. Density-functional theory calculations of 401 different prototypical structures and compositions spanning the $Co_xZn_{1-x}S$ solid solution space confirm that they are metastable with positive mixing enthalpies and formation energies that are 100-150 meV per formula unit above the convex hull. Competition experiments reveal preferential exchange of Co^{2+} vs. Zn^{2+} when both are present in excess. We balance their reactivities by controlling the ratio of total cations to copper sulfide, thereby avoiding the formation of cobalt sulfide byproducts. UV-visible absorption spectra reveal a decrease in band gap as x in $Co_xZn_{1-x}S$ increases; $x = 0.25$ and $x = 0.50$ are semiconducting while $x = 0.75$ is metallic. The optical properties of the $Co_xZn_{1-x}S$ solid solutions differ from CoS–ZnS heterostructures, which have similar compositions but different mixing behavior. The $Co_xZn_{1-x}S$ solid solution can also be integrated into heterostructured nanorods to combine their composition-tunable properties with other materials.

INTRODUCTION

Solid solutions, which homogeneously mix two or more end member compounds in a single phase, provide a platform for tuning the properties of materials in applications that include optoelectronics,[1] catalysis,[2] magnetism,[3] and energy storage.[4] Nanoparticles of mixed metal sulfides having the general formula $A_xB_{1-x}S$, *i.e.*, solid solutions of *A*S and *B*S, are particularly important. For example, quantum dots of cadmium–zinc chalcogenides such as $Cd_{1-x}Zn_xS$ have long been of interest because their bandgaps and optical properties depend both on their compositions and their sizes.[5–7] Copper indium gallium chalcogenides, including $CuIn_xGa_{1-x}S_2$, have been investigated as less toxic alternatives to Cd-, Pb-, and Hg-based quantum dots to achieve tunable optical properties within a single class of materials.[8,9] The synthesis of such solid solution nanoparticles can be challenging because of competition between forming the $A_xB_{1-x}S$ solid solution versus forming a mixture of the *A*S and *B*S end members. This competition is even more problematic when the solid solution is metastable and the end members are stable, as formation of the end members is much more favorable than formation of the solid solution.

Designing syntheses to target the formation of solid solution nanoparticles requires balancing the reactivities of the reagents so that they all combine as the nanoparticles are forming rather than first forming the individual end members. This outcome can be challenging to achieve because it relies on several interconnected reaction parameters that include the reactivities of the reagents (individually and with each other), temperature, time, concentration, surfactants, and solvents, as well as their interrelationships.[10] When targeting metal sulfide solid solutions, this synthetic challenge manifests as the need to balance the reactivities of *A* and *B* with a sulfur reagent to form $A_xB_{1-x}S$ while avoiding the formation of *A*S, *B*S, and/or mixed metal sulfides with different compositions than those targeted due to incomplete incorporation of *A* or *B*. Relevant considerations include the identities of the *A*, *B*, and sulfur reagents and whether or not their reactivities can be appropriately controlled within the available parameter space. If successful, these parameters often must be reoptimized for every composition in the solid solution as x in $A_xB_{1-x}S$ is varied with little ability to generalize, ultimately impeding the syntheses of compositionally tunable materials.

Cation exchange provides a convenient and potentially more generalizable strategy for synthesizing solid solution metal sulfide nanoparticles.[11,12] Cation exchange reactions modify the composition of a pre-synthesized nanoparticle without altering its morphology. This process inherently minimizes the number of independent synthetic parameters so that only the reactivities of the metal cations, which are intended to mix in the solid solution, must be considered. In a typical cation exchange reaction, the template nanoparticle, which for metal sulfides is often a copper compound such as roxbyite $Cu_{1.8}S$, will be introduced to a solution containing divalent or trivalent metal cations and a soft base, such as trioctylphosphine (TOP), that will solvate the softer Cu^+ cations in $Cu_{1.8}S$ so that the harder cations in solution can enter and diffuse through the nanoparticle.[13–19,] Preferential hard-hard and soft-soft interactions between the metal cations, which are Lewis acids, and bases such as TOP in solution provide a chemical driving force, and the copper-deficient $Cu_{1.8}S$ with high vacancy concentrations facilitates rapid cation diffusion.[12,20] Because of how they occur, cation exchange reactions generally retain the anion structure[21,22] and the morphology of the template nanoparticle[23] in the product.

The simplest solid solution metal sulfides have ternary compositions, such as for the generic $A_xB_{1-x}S$ compound. Most cation exchange routes to such mixed-metal sulfides form copper-based compounds derived from copper sulfides, produced by exchanging some of the Cu^+ cations with higher-valent cations to form $CuMS_x$ ($M = In^{3+}$, Ga^{3+}, Fe^{3+}, Sn^{4+}).[24–30] These syntheses also tend to produce small (< 10 nm) particles that are nominally spherical.[26,27] The formation of non-copper based solid solutions by cation exchange has been demonstrated for bulk miscible mixed-chalcogen systems that include $Cd_xZn_{1-x}S/Cd_yZn_{1-y}Se$ rod/dumbbell particles[1] and $Cd_xZn_{1-x}Se$ nanoplates.[31] In the former, a thiol surfactant was required to lower the reactivity of the Cd^{2+} reagent relative to the Zn^{2+} reagent, allowing the two cations to react simultaneously and form a single solid solution phase.[1] In the latter, cation exchange is utilized to generate CdSe@ZnSe core@shell particles, which are then annealed to form a $Cd_xZn_{1-x}Se$ solid solution.[31]

Nanoparticle cation exchange reactions with multiple metal salts are most commonly performed partially and sequentially, leading to the formation of heterostructured products that have multiple different metal sulfides interfaced together within the same particle.[18,32,33] For example, partial exchange of the Cu^+ cations in $Cu_{1.8}S$ nanorods with Cd^{2+} and then Zn^{2+} produces CdS–ZnS heterostructured nanorods.[18,33] Similarly, sequential partial exchange with Zn^{2+}, Co^{2+}, Ga^{3+}, and In^{3+} produces $ZnS–CoS–CuGaS_2–CuInS_2–Cu_{1.8}S$ heterostructured nanorods.[32] In contrast, simultaneous multi-cation exchange of $Cu_{1.8}S$ nanoparticles with Cd^{2+}/Zn^{2+} and $Zn^{2+}/Co^{2+}/Ga^{3+}/In^{3+}$ has been shown to produce $Cd_{1-x}Zn_xS$ and (Zn,Co,Ga,In,Cu)S solid solution nanoparticles, respectively[1,24]. This level of control over cation mixing—heterogeneously to form multi-component products versus homogeneously to form solid solutions—is powerful for controlling and tuning composition and is an emerging capability in nanoparticle cation exchange, but remains underexplored.

In a recent set of combinatorial multi-cation exchange experiments, we observed the formation of several metal sulfide solid solutions as components of more complex heterostructured nanorods, including $Ni_xCo_{9-x}S_8$, $Cd_xZn_{1-x}S$, $Co_xZn_{1-x}S$, and (Cu,In,Ga)S.[34] These observations suggest that solid solutions may be more broadly accessible through cation exchange. However, as that work was largely observational, we did not investigate the chemistry that led to the formation of solid solution components *via* simultaneous multi-cation exchange, nor did we consider composition tunability or the ability to target metastable solid-solution compositions, which are among the most difficult to synthesize by traditional routes. In that regard, the zinc cobalt sulfide solid solution, $Co_xZn_{1-x}S$, provides an instructive example. This mixed-metal sulfide has been synthesized though predominately hydrothermal methods for applications in electrochemical storage.[4,35–38] These $Co_xZn_{1-x}S$ nanoparticles have been made in a variety of morphologies but only with a composition of $Co_{0.24}Zn_{0.76}S$ and with a zincblende crystal structure, which is the most stable polymorph of the ZnS end member. To our knowledge, other Co-Zn-S compositions have not been reported. $Co_xZn_{1-x}S$ materials with very low amounts of Co^{2+} are also of interest as magnetic semiconductors.[39]

Here, we demonstrate the synthesis of composition-tunable $Co_xZn_{1-x}S$ solid solution nanoparticles using simultaneous Zn^{2+}/Co^{2+} cation exchange of roxbyite $Cu_{1.8}S$. The nominally hexagonal close packed (hcp) anion structure of the roxbyite template is retained in the $Co_xZn_{1-x}S$ solid solution products that adopt the wurtzite crystal structure, which is metastable for both the ZnS and CoS end members. Calculations using density-functional theory (DFT) confirm that the $Co_xZn_{1-x}S$ solid solution is also metastable, and we find that it is synthetically accessible using multi-cation exchange. The visible absorption features observed across $Co_xZn_{1-x}S$ solid solution members with x = 0.25, 0.50, and 0.75 change with composition, with decreasing bandgaps as the cobalt content increases, ultimately changing from semiconducting (x = 0.25 and 0.50) to metallic (x = 0.75). Successful synthesis of $Co_xZn_{1-x}S$ solid solution nanoparticles with tunable compositions, as well as avoidance of end member formation, is achieved by balancing the reactivity of the Zn^{2+} and Co^{2+} cations. The $Co_xZn_{1-x}S$ solid solution is then incorporated as a segment in a heterostructured $Co_xZn_{1-x}S$–$Cu_{1.8}S$ nanorod, demonstrating that the balanced reactivities of the metal salt solutions are portable to partial cation exchange reactions.[13,32] This result merges two distinct ways of mixing cations—heterogeneously as a heterostructured nanoparticle and homogeneously as a solid solution—to expand capabilities in the design and synthesis of compositionally complex nanoparticles.

EXPERIMENTAL SECTION

Chemicals. Benzyl ether [99%] was purchased from Acros Organics. Octadecene [ODE, 90%, technical grade], technical grade oleylamine [tg-OLAM, 70%], tert-dodecanethiol [t-DDT, mixture of isomers 98.5%], 1-dodecanethiol [DDT, ≥98%], di-*tert*-butyl-disulfide [97%], copper(II) nitrate trihydrate [$Cu(NO_3)_2 \cdot 3H_2O$, puriss. p.a. 99-104%], trioctylphosphine oxide [TOPO, ≥90%], copper(II) chloride [$CuCl_2$, 97%], zinc chloride [$ZnCl_2$, ≥ 97% ACS reagent grade, anhydrous], and cobalt(II) chloride [$CoCl_2$, 97%] were purchased from Sigma Aldrich. Trioctylphosphine [TOP, >85%] was purchased from TCI America. All solvents, including hexanes, toluene, isopropyl alcohol [IPA], and acetone were of analytical grade. All the above chemicals were used as received without further purification. Distilled oleylamine (d-OLAM) was prepared from tg-OLAM, using an established procedure.[32]

Synthesis of $Cu_{1.8}S$ nanoparticles. Roxbyite $Cu_{1.8}S$ spheres[18] plates,[17,23] and rods[32] were synthesized following modifications of the cited published procedures. Complete details are provided in the Supporting Information.

Simultaneous cation exchange to form solid solution nanoparticles. Simultaneous cation exchange reactions followed a modification of a published procedure.[24] In a typical synthesis of $Zn_{0.5}Co_{0.5}S$ nanoparticles, 0.467mL of 730 mM $ZnCl_2$ and 1.100mL of 310 mM $CoCl_2$, both in a mixure of benzyl ether, tg-OLAM, and ODE (prepared as described in the Supporting Information and Table S1), were added to a round bottom flask equipped with a reflux condenser, gas flow adapter, alcohol thermometer, rubber septum, and magnetic stir bar. Then, 7.5 mL of benzyl ether, 4 mL of tg-OLAM, and 1 mL of ODE were added to the flask. While stirring, this mixture was placed under vacuum, heated to 100 °C, and held at this temperature for 30 minutes. Then, the mixture was placed under a blanket of Argon (Ar) after cycling between vacuum and Ar three times. $Zn_xCo_{1-x}S$ nanoparticles having other compositions were prepared by adjusting the amounts of the $ZnCl_2$ and $CoCl_2$ solutions, as described in the Supporting Information[40]. Meanwhile, 3 mL of TOP was transferred (air-free) to a vial containing 18 mg of $Cu_{1.8}S$ nanoparticles (under Ar). (The morphologies of the $Zn_xCo_{1-x}S$ nanoparticles are dependent upon the morphologies of $Cu_{1.8}S$ templates, *i.e.*, spheres, plates, or rods.) This suspension was placed under a blanket of Ar after cycling between vacuum and Ar 2-3 times. The vial containing the suspension was then sonicated for at least 45 minutes. The $Cu_{1.8}S$/TOP suspension was injected rapidly at 100 °C and the reaction was allowed to proceed for 30 minutes before placing the flask in an ice bath. Once the temperature in the flask reached ~10-20 °C, the resulting product was precipitated by the addition of a 1:1 mixture of IPA/acetone followed by centrifugation (13,500 rpm for 3 min) and resuspension in toluene. This centrifugation/resuspension process was completed one more time before dispersing the particles in toluene. The morphologies of the $Zn_xCo_{1-x}S$ nanoparticles match the morphologies of the $Cu_{1.8}S$ nanoparticle templates.

<u>Sequential cation exchange to form heterostructured nanoparticles</u>. Sequential cation exchange reactions followed a modification of a published procedure.[32] In a typical synthesis of heterostructured ZnS–CoS nanoparticles containing approx. 50% ZnS and 50% CoS, 0.467mL of 730 mM $ZnCl_2$ was added to a round bottom flask equipped with a reflux condenser, gas flow adapter, alcohol thermometer, rubber septum, and magnetic stir bar. Then, 7.5 mL of benzyl ether, 4 mL of tg-OLAM, and 1 mL of ODE were added to the flask. While stirring, this mixture was placed under vacuum, heated to 100 °C, and held at this temperature for 30 minutes. Then, the mixture was placed under a blanket of Ar after cycling between vacuum and Ar three times. Different heterostructured nanoparticles having other compositions were prepared by adjusting the amount of the $ZnCl_2$ solution added in this step, as described in the Supporting Information. Meanwhile, 3 mL of TOP was transferred (air-free) to a vial containing 18 mg of spherical $Cu_{1.8}S$ nanoparticles (under Ar). This suspension was placed under a blanket of Ar after cycling between vacuum and Ar 2-3 times. The vial containing the suspension was then sonicated for at least 45 minutes. The $Cu_{1.8}S$/TOP suspension was injected rapidly at 100 °C and the reaction was allowed to proceed for 30 minutes. Then, 4.00 mL of 310 mM $CoCl_2$ was injected (air-free) into the flask. (Note that the $CoCl_2$ solution will turn red after sitting in air for multiple days; the solution was heated with a heatgun until it turned from red to blue before injection.) This reaction was allowed to proceed for 30 minutes before placing the flask in an ice bath. Once the temperature in the flask reached ~10-20 °C, the resulting product was precipitated by the addition of a 1:1 mixture of IPA/acetone followed by centrifugation (13,500 rpm for 3 min) and resuspension in toluene. This centrifugation/resuspension process was completed one more time before dispersing the particles in toluene.

First-principles calculations. Simulations were performed within the Perdew–Burke–Ernzerhof (PBE) parameterization[41] of the generalized-gradient approximation (GGA),[42–44] implemented in the Quantum-ESPRESSO software.[45,46] Ionic cores were described using norm-conserving Vanderbilt pseudopotentials.[47–49] The ***k***-point resolution in the first Brillouin zone was set to 0.05 $Å^{-1}$ and the kinetic energy cutoff was set to 80 Ry with a charge density cutoff of 320 Ry. These cutoffs were chosen so that the total energy and forces were converged within 1.0 meV and 25 meV/A, respectively. The self-consistent field threshold was set to 10^{-10} Ry. To predict cation ordering in $Zn_{1-x}Co_xS$, a convex hull was constructed. Here, a total of 401 symmetrically unique wurtzite configurations up to a size of eight formula units were generated using the structure enumeration module[50,51] within the Integrated Cluster Expansion Toolkit (ICET) Python package.[52] These structures were then fully relaxed via geometry optimization with energy and force convergence thresholds of 10^{-5} Ry and 10^{-4} Ry/bohr, respectively. The mixing enthalpies of these structures were calculated as $\Delta H = H_{(Zn,Co)S} - (1 - x) H_{ZnS} - x H_{CoS}$, where x is the Co concentration, $H_{(Zn,Co)S}$ is the energy of a configuration per formula unit, and H_{ZnS} and H_{CoS} are the reference energies of ZnS and CoS, respectively.

Characterization. Transmission electron microscopy (TEM) images were collected on a FEI Tecnai G20 XTWIN microscope operating at 200kV. High angle annular dark field scanning TEM (HAADF-STEM) and STEM energy dispersive X-ray spectroscopy (STEM-EDS) maps were collected on a FEI Talos F2000X S/TEM at an accelerating voltage of 200kV. Bruker ESPRIT 2 software was used to interpret the STEM-EDS element map data. The EDS lines used were S Kα, Zn Kα, Co Kα, and Cu Kα. All samples that were analyzed by EDS were cast onto Ni TEM grids. ImageJ software was used to measure particle dimensions from the TEM images. Powder X-ray diffraction (XRD) data were collected on a Malvern PANalytical Empyrean I using Cu Kα radiation. UV-Vis-NIR absorption data were collected on a Perkin Elmer LAMBDA 950 UV-Vis NIR spectrometer using a standard detector and a quartz spectrophotometer cell from Starna Cells, Inc. with a data interval of 2 nm. Samples measured from 850-300 nm were prepared in toluene and sonicated for approximately 5 minutes before data collection. Samples measured from 300-2000 nm were prepared in tetrachloroethylene and sonicated for approximately 5 minutes before data collection. All simulated diffraction patterns were generated using CrystalDiffract and all crystal structures[53–57] shown were generated using CrystalMaker, distributed by CrystalMaker Software Ltd, Oxford, England (www.crystalmaker.com).

RESULTS AND DISCUSSION

Synthesis and characterization of spherical $Co_xZn_{1-x}S$ nanoparticles

It is known that simultaneous cation exchange can lead to solid solution formation and/or phase segregation and heterostructuring, based on a confluence of the identity of the incoming cation(s), the reactivity of the incoming cation(s), the composition of the template particle, and the shape and size of the template particle.[34] This presents a fundamentally interesting scenario where multiple outcomes are possible from a single simultaneous cation exchange reaction. Simultaneous multi-cation exchange is therefore important for understanding how to control composition and composition distributions in complex nanoparticle systems. Accordingly, we began by carrying out simultaneous complete exchange of the Cu^+ cations in nominally spherical roxbyite $Cu_{1.8}S$ nanoparticles, having an average diameter of 21 ± 1 nm (n = 150) (Figures 1a and S1), with mixtures of Zn^{2+} and Co^{2+} in different ratios. A suspension of $Cu_{1.8}S$ nanoparticles in TOP were injected into a flask at 100 °C under Ar that contained $ZnCl_2$ and $CoCl_2$ in ratios of 3:1, 1:1, and 1:3 dissolved in a mixture of benzyl ether, octadecene, and oleylamine to span a wide range of potential solid solution compositions (Figure 1b). Figure 1c shows HAADF-STEM images for the products of each exchange reaction and reveals that the nominally spherical morphology of the $Cu_{1.8}S$ nanoparticles was retained.

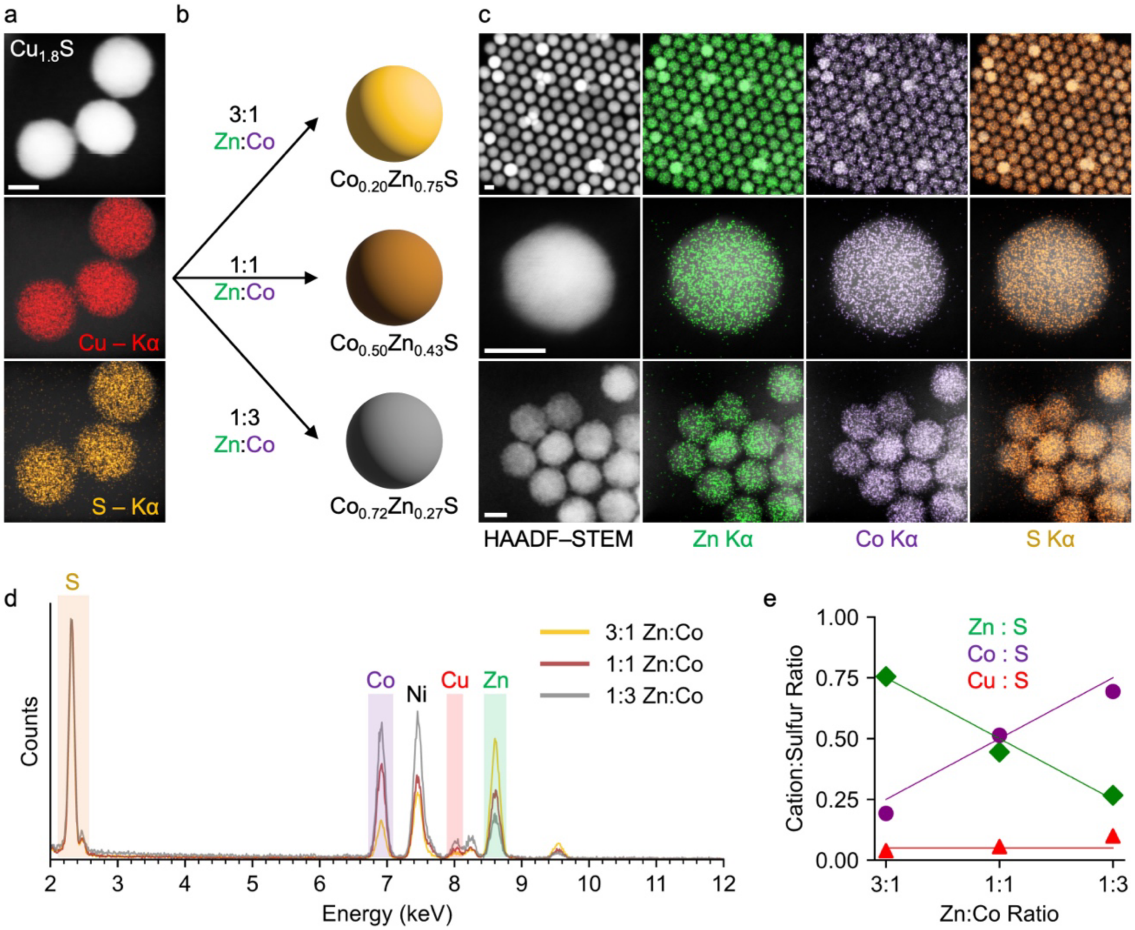

Figure 1. (a) HAADF-STEM image and STEM-EDS element maps for Cu and S (shown overlaid on the HAADF-STEM image) of the spherical $Cu_{1.8}S$ nanoparticle templates. (b) Reaction schematic showing the spherical $Cu_{1.8}S$ nanoparticles undergoing simultaneous Zn^{2+}/Co^{2+} cation exchange with different ratios of $ZnCl_2$:$CoCl_2$ to yield compositionally different $Co_xZn_{1-x}S$ products. (c) HAADF-STEM images and STEM-EDS element maps for Zn, Co, and S (shown overlaid on the HAADF-STEM images) for all three $Co_xZn_{1-x}S$ products: 3:1 Zn:Co (top), 1:1 Zn:Co (middle), and 1:3 Zn:Co (bottom). (d) EDS spectra for all three compositions (on Ni TEM grids), normalized to sulfur. (e) Plot of cation to sulfur ratios (from the EDS spectra) for all three Zn:Co compositions. (Zn:S = green diamonds, Co:S = purple spheres, Cu:S = red triangles.) For the Zn:S and Co:S values, the lines show the expected cation:sulfur ratios based on the $ZnCl_2$:$CoCl_2$ loadings. For the Cu:S value, the line is fixed at 5%, which is considered to be the approximate residual amount of copper after exchange. All scale bars are 10 nm.

STEM-EDS imaging also confirms that Co and Zn are uniformly distributed throughout the fully-exchanged particles. STEM-EDS element maps for samples having 3:1, 1:1, and 1:3 Zn:Co ratios, shown in Figures 1c and Figures S2-4, reveal homogeneous co-localization of Zn, Co, and S across all particles. Quantification of the corresponding STEM-EDS spectra (Figure 1d) indicates that the compositions of the nominal 3:1, 1:1, and 1:3 Zn:Co solid solution samples are $Zn_{0.75}Co_{0.20}S$, $Zn_{0.43}Co_{0.50}S$, and $Zn_{0.27}Co_{0.72}S$, respectively. The composition data, which are plotted in Figure 1e, show how the cation:sulfur ratio of the product compares to the ratio expected based on the composition of the exchange solution. The sum of the cations relative to sulfur is nearly 1:1 in all cases, although as is common during cation exchange, very small amounts of Cu^+ may remain.[13] The actual composition therefore matches well with the expected composition based on the $ZnCl_2$:$CoCl_2$ ratio used during simultaneous cation exchange.

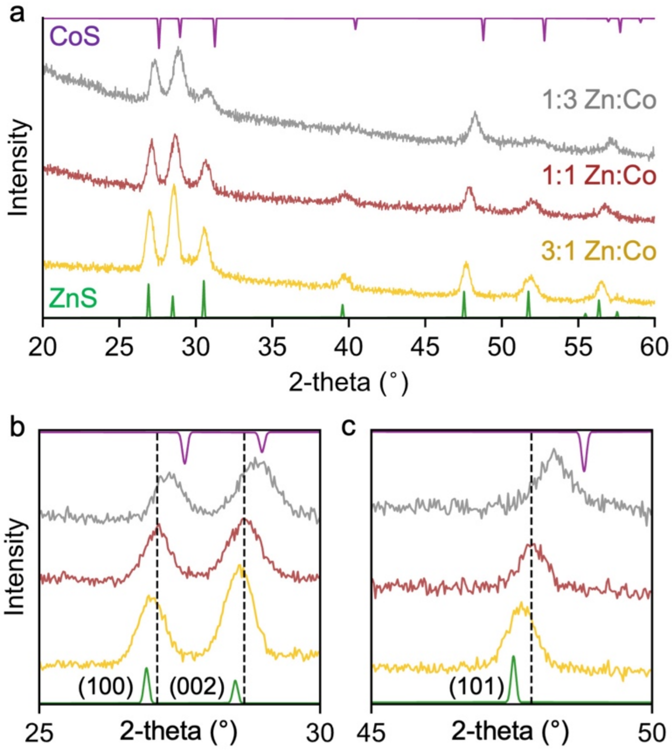

Figure 2. (a) Powder XRD patterns for the 3:1, 1:1, and 1:3 Zn:Co compositions of the spherical $Co_xZn_{1-x}S$ nanoparticles (x = 0.75 is grey, x = 0.5 is brown, and x = 0.25 is yellow). Reference XRD patterns for wurtzite ZnS[53] (green) and wurtzite CoS[54] (purple) are shown for comparison. Enlarged regions of the XRD patterns in (a) are shown in (b) from 25 – 30°, highlighting the (100) and (002) peaks, and in (c) from 45 – 50°, highlighting the (101) peak.

Figure 2a shows powder XRD patterns for the products isolated from the reactions having 3:1, 1:1, and 1:3 $ZnCl_2$:$CoCl_2$ ratios, along with reference patterns for wurtzite ZnS and wurtzite CoS for comparison. The experimental XRD patterns are consistent with a single wurtzite phase, but all are shifted relative to the parent structures. An enlarged region showing the (100) and (002) reflections (Figure 2b) and the (101) reflection (Figure 2c) demonstrates the progressive shift to the right, and therefore a progressive decrease in lattice constant, moving from the 3:1 to 1:1 to 1:3 Zn:Co ratios, as is expected for the composition variation in $Co_xZn_{1-x}S$, given the larger ionic radius of Zn^{2+} versus that of Co^{2+}.[58] For solid solutions, the lattice parameters can often be described as an average of the lattice parameters of the parent phases weighted by composition, assuming that the crystal structures are the same. The hexagonal unit cell of wurtzite ZnS (a = 3.82 Å, c = 6.26 Å)[53] has larger lattice parameters than that of wurtzite CoS (a = 3.72 Å, c = 6.16 Å).[54,59] The lattice parameters for the $Co_xZn_{1-x}S$ solid solutions follow the expected trend of decreasing lattice constants with increasing Co^{2+} content: for 3:1 Zn:Co, a = 3.81 Å and c = 6.24 Å; for 1:1 Zn:Co, a = 3.80 Å and c = 6.22 Å; and for 1:3 Zn:Co, a = 3.77 Å and c = 6.17 Å. Wurtzite patterns incorporating these experimentally determined lattice parameters match well to XRD patterns for the three products (Figure S5). The XRD and STEM-EDS data therefore confirm the formation of single-phase composition-tunable $Co_xZn_{1-x}S$ solid solutions, with nanoparticle composition being controlled and tuned simply by changing the ratio of the metal salts used in the simultaneous cation exchange reaction.

Stability of the $Co_xZn_{1-x}S$ solid solution

Complete exchange of the Cu^+ cations in roxbyite $Cu_{1.8}S$ with Zn^{2+} is known to produce wurtzite ZnS[13,21] while Co^{2+} exchange can produce either wurtzite CoS or pentlandite Co_9S_8, depending on the size of the $Cu_{1.8}S$ template nanoparticles.[16,17,54] The wurtzite end members of the $Co_xZn_{1-x}S$ solid solution, CoS and ZnS, are therefore accessible by cation exchange, although both are metastable. The thermodynamically most stable polymorph of ZnS is zincblende, but the wurtzite phase forms during cation exchange because the sulfur anions in the template $Cu_{1.8}S$ nanoparticles adopt a slightly distorted hexagonally close packed (HCP) arrangement, which is retained (undistorted) upon cation exchange. Wurtzite CoS is similarly metastable and forms through analogous structure retention during cation exchange.[54]

DFT calculations were used to study the stability of the $Co_xZn_{1-x}S$ solid solution. A total of 401 symmetrically unique configurations of up to eight formula units of $Co_xZn_{1-x}S$ were generated from derivative structures of a host lattice.[50,51] These configurations span different cell shapes and sizes while imposing the wurtzite structure. Figure 3 shows the mixing enthalpies (ΔH_{mix}) of these structures plotted with the first-principles convex hull of the wurtzite $Co_xZn_{1-x}S$ solid solution members with x = 0, 0.125, 0.25, 0.375, 0.5, 0.625, 0.75, 0.875, and 1; x = 0 and x = 1 correspond to the wurtzite ZnS and wurtzite CoS end members, respectively. Crystal structures of the lowest-energy configurations are shown in Figures 3 and S6. These structures exhibit some Co ordering and distortions due largely to enhanced Co-Co bonding. Except for one configuration at x = 0.875, all members of the wurtzite $Co_xZn_{1-x}S$ solid solution have positive mixing enthalpies and therefore most configurations are metastable at 100-150 meV/f.u. above the convex hull. These values are positive, indicating that both the $Co_xZn_{1-x}S$ solid solution and the CoS and ZnS end members are metastable while being synthetically accessible through simultaneous multi-cation exchange.

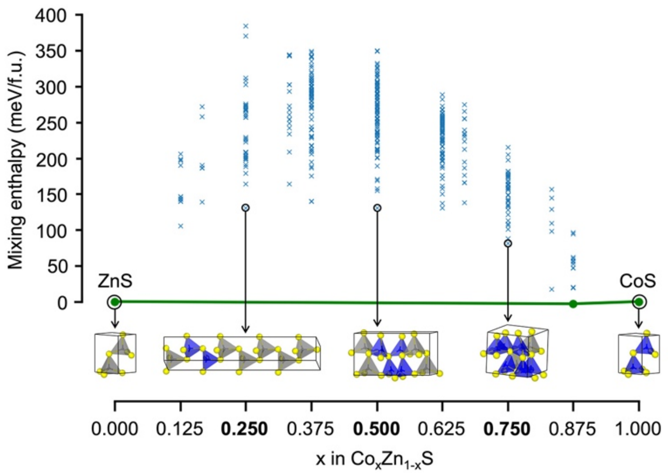

Figure 3. Plot of the constructed convex hull, shown as green filled circles (●), for a solid solution between ZnS ($x = 0$ in $Co_xZn_{1-x}S$) and CoS ($x = 1$ in $Co_xZn_{1-x}S$). This construction determines which structures are stable, metastable, or unstable. Each blue data point (×) represents one of the 401 structural enumerations. Structures with the lowest energy at fixed Co compositions of x = 0.0, 0.25, 0.50, 0.75, and 1.00 are shown. Zinc is gray, cobalt is blue, and sulfur is yellow. All structural representations above $\Delta H_{mix} = 0$ have a positive enthalpy of mixing.

Chemical insights into the reaction

As discussed in the preceding sections, formation of the $Co_xZn_{1-x}S$ solid solution was not an obvious outcome of simultaneous cation exchange, given the competition between homogeneous solid solutions and phase segregated heterostructures that both have been observed as products during such reactions,[24,34] as well as its metastability. This suggests that there are likely to be key aspects of the reaction that define the pathways that lead to formation of phase segregated ZnS–CoS heterostructures versus $Co_xZn_{1-x}S$ solid solutions. With this in mind, reaction conditions were systematically varied to identify the key conditions for selectively generating solid solutions and heterostructures. We began by varying the total amount of $ZnCl_2$ and $CoCl_2$ in the reaction. Figure 1 showed the products that formed when using a 1.1:1 molar ratio of total cations to $Cu_{1.8}S$, *i.e.*, a nearly stoichiometric reaction with a slight excess of cations to ensure complete exchange. In contrast, Figure 4 shows data for a series of reactions having Zn:Co ratios of 3:1, 1:1, and 1:3 but with a molar ratio of total incoming cations to copper sulfide of 4.

For the reaction that uses a 3:1 ratio of Zn:Co and a molar ratio of total cations to copper sulfide of 4, the XRD (Figure S7) and STEM-EDS (Figure 4 and S8ab) data show the formation of a solid solution having a composition (from EDS analysis) of $Co_{0.44}Zn_{0.49}S$ instead of the expected $Co_{0.25}Zn_{0.75}S$ (Figure S9). This result indicates that, under these conditions of reaction temperature and time, Co^{2+} is more reactive and therefore outcompetes Zn^{2+} during the exchange, as Co^{2+} is enriched in the product despite the significant excess of Zn^{2+} available. This observation is further validated by the results of the 1:1 Zn:Co reaction (still with a 4-fold molar excess of total incoming cations to $Cu_{1.8}S$), which generates two products: a wurtzite $Co_xZn_{1-x}S$ solid solution and Co_9S_8 (Figure 4). These two products were identified by XRD, where we find evidence of both Co_9S_8 and the wurtzite solid solution (Figure S7), and in the STEM-EDS element maps, where some particles have only Co signal while others have colocalized Zn and Co signals (Figures 4 and S8cd). (Note that Co^{2+} exchange on $Cu_{1.8}S$ spheres is known to produce a mixture of wurtzite CoS and pentlandite Co_9S_8;[16,17] we classify the observed cobalt sulfide that does not contain zinc as Co_9S_8, based on XRD, but note that some CoS could also be forming.[16]) Finally, when a 1:3 Zn:Co ratio is used while the molar ratio of total cations to $Cu_{1.8}S$ is 4, the product is almost entirely Co_9S_8, with only a minor amount of the wurtzite $Co_xZn_{1-x}S$ solid solution, based on analysis of the XRD (Figure S7) and STEM-EDS (Figures 4 and S8e) data.

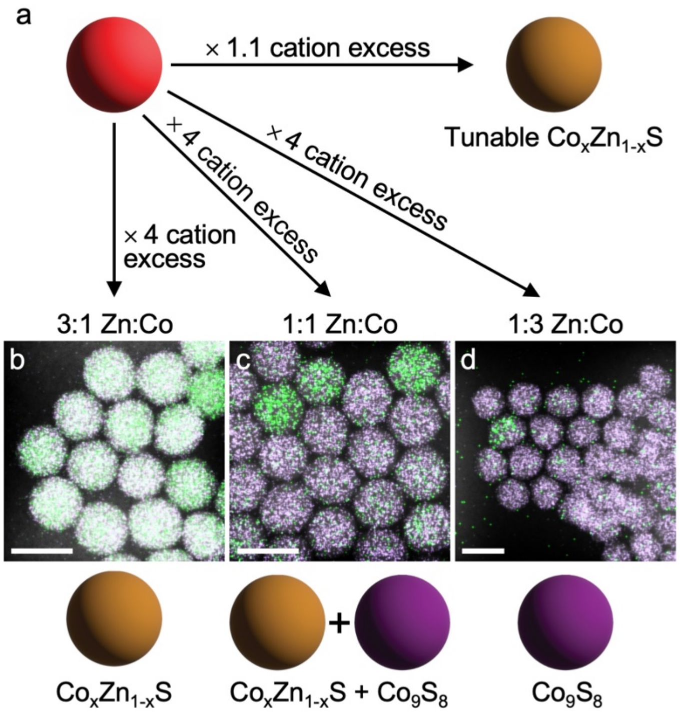

Figure 4. (a) Reaction diagram depicting the different outcomes that occur based on the ratio of total cations to copper sulfide. The 1.1:1 excess corresponds to the data in Figure 1. STEM-EDS element maps (green = Zn, purple = Co) superimposed on HAADF-STEM images for the fourfold total cation excess are shown in (b) for the 3:1 Zn:Co ratio, in (c) for the 1:1 Zn:Co ratio, and in (d) for the 1:3 Zn:Co ratio. The drawings at the bottom highlight that at high ratios of total cations to nanoparticles, the formation of cobalt sulfide nanoparticles becomes more prevalent, indicating Co^{2+} outcompetes Zn^{2+}. All scale bars are 20 nm.

These experiments described in Figure 4 demonstrate that the composition of the solid solutions formed in the initial experiment (Figure 1) matched the Zn:Co ratio of the exchange solution because the ratio of total cations to copper sulfide nanoparticles was close to 1, which served to balance the inherent reactivity mismatch between Zn^{2+} and Co^{2+} in solution. The difference in reactivity between Co^{2+} and Zn^{2+} with respect to forming Co_9S_8 versus a $Co_xZn_{1-x}S$ solid solution is small and surprising, as previous reports describe near identical reactivities based on the threshold temperatures at which they undergo cation exchange.[18,32,34] However, at higher concentrations of these cations, *i.e.*, when the molar ratio of total cations to $Cu_{1.8}S$ is significantly greater than 1, this small difference in reactivity is magnified, resulting in competition and ultimately the formation of two distinct products: both Co_9S_8 and $Co_xZn_{1-x}S$ (Figure 4). Cation reactivity has been invoked to tune between phase segregated and solid solution products.[1,24] To summarize, the similar reactivities of Co^{2+} and Zn^{2+} can be exploited to generate solid solutions at low molar ratios of total cations to copper sulfide, but Co^{2+} is slightly more reactive and using reaction conditions that magnify this difference in reactivity, the reaction outcome can be driven away from solid solution formation (Figure 4).

Morphological insights into the reaction

Copper sulfide nanoparticle morphology is also known to play a role in the outcomes of cation exchange reactions, particularly involving Zn^{2+} and Co^{2+}. Exchanges with Co^{2+} result in different products, either Co_9S_8 (cubic close packed) or wurtzite CoS (hexagonal close packed), depending on the morphology of the $Cu_{1.8}S$ nanoparticle template.[16,24] For morphologies where the particle dimension is small (<7 nm) in the direction in which the pseudo-closed packed planes of sulfur anions in $Cu_{1.8}S$ stack, wurtzite CoS forms, whereas when the $Cu_{1.8}S$ particle dimension is larger (>13 nm) in this same crystallographic direction, Co_9S_8 forms.[24] For exchanges with Zn^{2+}, a related phenomenon occurs. For morphologies of $Cu_{1.8}S$ where the direction in which the pseudo-closed packed planes of anions stack is large, stacking fault formation is observed in the wurtzite ZnS product.[60] These stacking faults represent lateral shifts in the closed pack planes of sulfur anions in wurtzite ZnS, effectively disrupting the hexagonal close packed stacking sequence, *ABAB*, with regions of cubic close packing, *ABCABC*. Because these two cation exchange reactions have different outcomes for different morphologies, we also studied the effect of morphology on solid solution formation during simultaneous multi-cation exchange.

Nanoplates of djurleite copper sulfide (7 ± 1 nm × 120 ± 20 nm, n = 150) (Figure S10) and nanorods of roxbyite copper sulfide (57 ± 5 nm × 21 ± 1 nm, n = 150) (Figure S10) were synthesized and then used as templates for simultaneous Zn^{2+}/Co^{2+} cation exchanges at 3:1, 1:1, and 1:3 Zn:Co ratios with an overall molar ratio of total cations to copper sulfide of 1.1, analogous to the experiments using spherical $Cu_{1.8}S$ nanoparticles, shown in Figure 1. The crystal structures of roxbyite ($Cu_{1.8}S$) and djurleite ($Cu_{1.94}S$) are nearly identical; both contain pseudo-hexagonal closed packed sulfur anions and differ only subtly in the coordination environments and stoichiometries of the Cu^+ cations.[61,62] Their core similarities, as related to cation exchange, allow us to consider morphology as the only consequential variable that differentiates these reactions from one another and from those carried out on the spherical nanoparticles described earlier.

The data in Figure 5 correspond to wurtzite $Co_xZn_{1-x}S$ nanoplates formed from simultaneous Zn^{2+}/Co^{2+} cation exchange using Zn:Co ratios of 3:1, 1:1, and 1:3. The XRD patterns (Figure 5a) indicate that the 3:1 and 1:1 Zn:Co ratio produces a single wurtzite phase with shifted peaks consistent with the expected changes in composition in the 3:1 and 1:1 Zn:Co ratios. By XRD, the 1:3 Zn:Co product has asymmetry in the (002) peak, suggesting that there may be a mixture of the 1:3 solid solution and wurtzite CoS. The STEM-EDS maps confirm the near-absence of Cu and co-localization Zn, Co, and S signals for the 3:1 and 1:1 samples (Figures 5b and S11a,b). For the sample made using a 1:3 Zn:Co ratio, the STEM-EDS maps confirm the presence of both the $Co_xZn_{1-x}S$ solid solution and CoS within particles (Figure 5b), as well as CoS plates with no Zn incorporation (Figure S11c), as suggested above based on XRD analysis. It is worth noting that the peak shapes and relative intensities in the XRD patterns in Figure 5a are consistent with the features expected for nanoplates. The (*hk*0) peaks, which correspond to the crystallographic planes that stack laterally across the widths of the nanoplates, are sharper than the (00*l*) peaks, which correspond to the planes that stack vertically. The (00*l*) peak is broad because the plates are only approx. 7 nm thick. At the same time, the relative intensities of these broad (00*l*) peaks are high because of preferred orientation, as the nanoplates preferentially lie flat on the sample holder (Figure 5c).

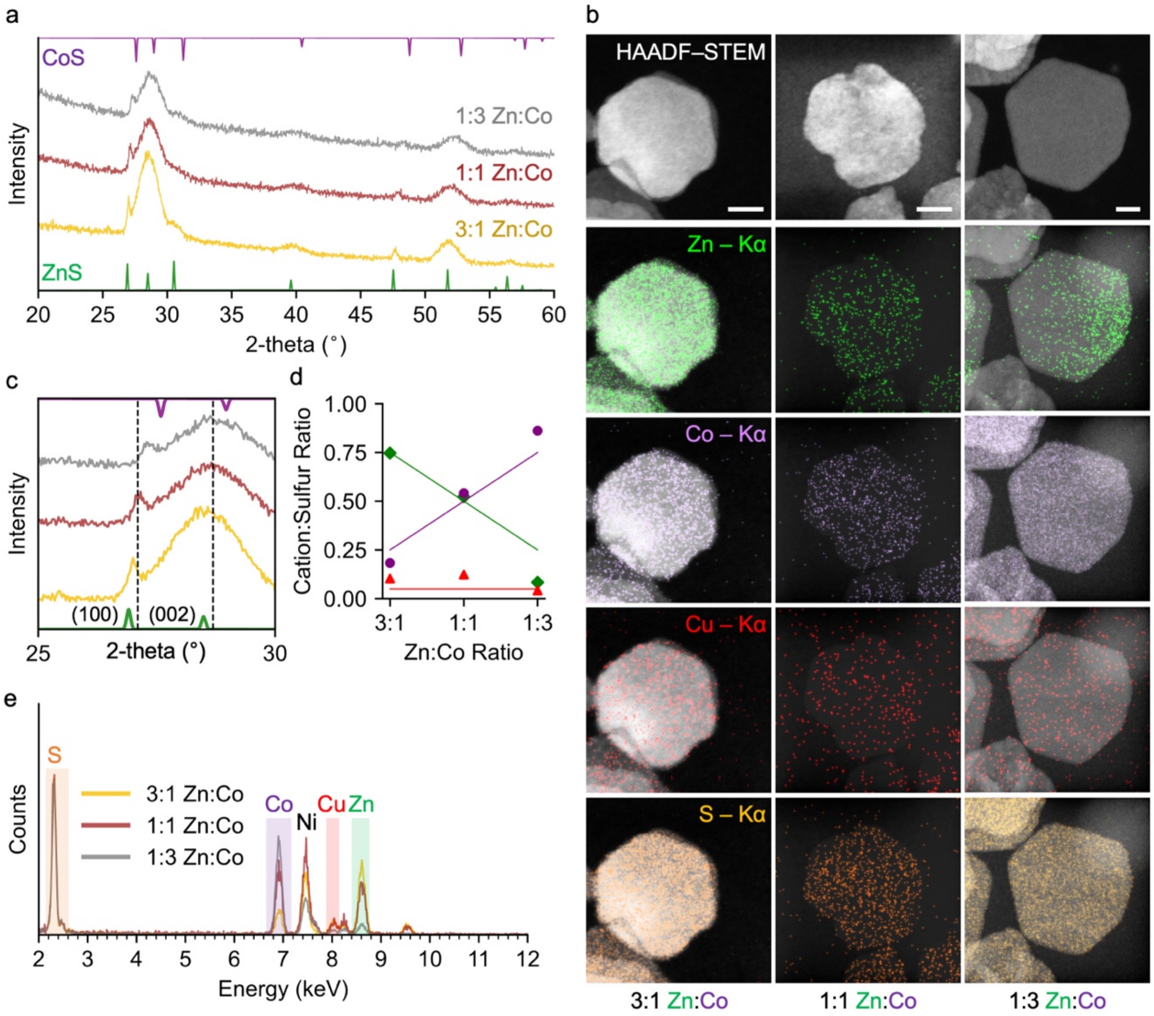

Figure 5. (a) Powder XRD patterns for the 3:1, 1:1, and 1:3 (bottom to top) Zn:Co simultaneous cation exchange reactions on $Cu_{1.94}S$ plates ($x = 0.75$ is grey, $x = 0.5$ is brown, and $x = 0.25$ is yellow). Reference XRD patterns for wurtzite ZnS[53] (green) and wurtzite CoS[54] (purple) are shown for comparison. (b) HAADF-STEM images and STEM-EDS element maps for Zn, Co, Cu, and S (shown overlaid on the HAADF-STEM images) for all three Zn:Co compositions: 3:1 Zn:Co (left), 1:1 Zn:Co (middle), and 1:3 Zn:Co (right). All scale bars are 10 nm. An enlarged region of the XRD pattern in (a) is shown in (c) from 25 – 30°, highlighting the (100) and (002) peaks. (d) Plot of cation to sulfur ratios (from the EDS spectra) for all three Zn:Co compositions. (Zn:S = green diamonds, Co:S = purple spheres, Cu:S = red triangles.) For the Zn:S and Co:S values, the lines show the expected cation:sulfur ratios based on the $ZnCl_2$:$CoCl_2$ loadings. For the

Cu:S value, the line is fixed at 5%, which is considered to be the approximate residual amount of copper after exchange. (e) EDS spectra for all three compositions (on Ni TEM grids), normalized to sulfur.

Quantification of the STEM-EDS maps (Figure 5d) and the corresponding spectra (Figure 5e) reveals that they follow a similar trend to the spherical nanoparticle products, with compositions of $Zn_{0.74}Co_{0.19}S$ and $Zn_{0.52}Co_{0.54}S$ for the 3:1 and 1:1 Zn:Co exchanges. These experimentally determined compositions are close to the compositions expected based on the $ZnCl_2$:$CoCl_2$ ratio. The formation of a $Co_xZn_{1-x}S$ solid solution during simultaneous Zn^{2+}/Co^{2+} exchange of the nanoplates, which have a thickness of approx. 7 nm, is consistent with the behavior of the end members, which also form wurtzite ZnS and CoS upon cation exchange of sub-7 nm $Cu_{1.8}S$ nanoparticles. Interestingly, formation of the solid solutions appears to be disfavored for nanoplates in the Co-rich 1:3 Zn:Co sample. This observation is not surprising given the data in Figure 4, which indicates that Co^{2+} is more reactive than Zn^{2+} when both are present in excess and can compete for exchange. This reactivity difference appears to be exacerbated by the anisotropy and/or larger size of the plates relative to the spheres, which formed $Co_xZn_{1-x}S$ solid solutions across all Zn:Co ratios.

Analogous nanorod systems, spanning all three Zn:Co ratios, are shown in Figure 6. As for the nanoplates, simultaneous Zn^{2+}/Co^{2+} exchange produced a single wurtzite pattern for the 3:1 and 1:1 Zn:Co ratios, while a mixture of the solid solution and Co_9S_8 is formed for the 1:3 Zn:Co ratio. The XRD data for the 3:1 and 1:1 Zn:Co products show a single phase wurtzite pattern with lattice parameters in between those of the two reference patterns (Figure 6a). The XRD pattern of the 1:3 Zn:Co product consists of Co_9S_8[56] along with a minor product of the wurtzite $Co_xZn_{1-x}S$ solid solution. Consistent with the XRD data, STEM-EDS element maps confirm the removal of Cu and the co-localization of Zn, Co, and S signals in the 3:1 and 1:1 products (Figures 6b and S12a,b). The STEM-EDS element maps for the 1:3 Zn:Co nanorod product appear to contain both Co_9S_8 and $Co_xZn_{1-x}S$ (Figure 6b and S12c). Analysis of the corresponding XRD patterns (Figure 6c) reveals that the (100) and (002) peaks of the 3:1 and 1:1 Zn:Co products follow the expected shifts, given contraction of the lattice with increasing Co content. The (100) peak is broad, as expected, since the planes (100) planes correspond to the width of the rods (21 nm). In contrast, the (002) peak is sharper, since the (002) planes correspond to the length of the rods (57 nm).

Quantification of the STEM-EDS data (Figure 6d) and the corresponding EDS spectra (Figure 6e) reveal a trend in composition for the nanorods that is analogous to that of the plates: the EDS composition is $Zn_{0.72}Co_{0.19}S$ for the 3:1 product and $Zn_{0.54}Co_{0.56}S$ for the 1:1 product. The formation of a wurtzite $Co_xZn_{1-x}S$ solid solution was expected for the nanoplates, as their thinnest dimension is in the range where the hexagonal close packed anion structure is known to persist during cation exchange with both Zn^{2+} and Co^{2+}. However, the formation of a wurtzite $Co_xZn_{1-x}S$ solid solution was unexpected for the nanorods, where Co^{2+} exchange has previously been shown to produce Co_9S_8 instead of CoS. The anions in Co_9S_8 adopt a ccp lattice and the cobalt exists in both tetrahedrally and octahedrally coordinated sites with some close Co–Co contacts that lead to metallic bonding. In contrast, the anions in wurtzite CoS and ZnS are hcp with cations present exclusively in tetrahedral sites. In terms of reactivity, the same reactivity observed for the plates is also observed for the rods, whereby exchanges with high Co^{2+}:Zn^{2+} ratios result in Co^{2+} outcompeting Zn^{2+} to produce regions of Co_9S_8 instead of exclusively the $Co_xZn_{1-x}S$ solid solution. The larger size and/or the anisotropy of the nanoplates and nanorods, coupled with the slightly higher reactivity of Co^{2+}, result in the formation of different products through cation exchange compared to the spherical products for the 1:3 Zn:Co reaction. This outcome is not unprecedented as identical cation exchange reactions on different morphologies of template nanoparticles has previously been observed to lead to different outcomes.[34]

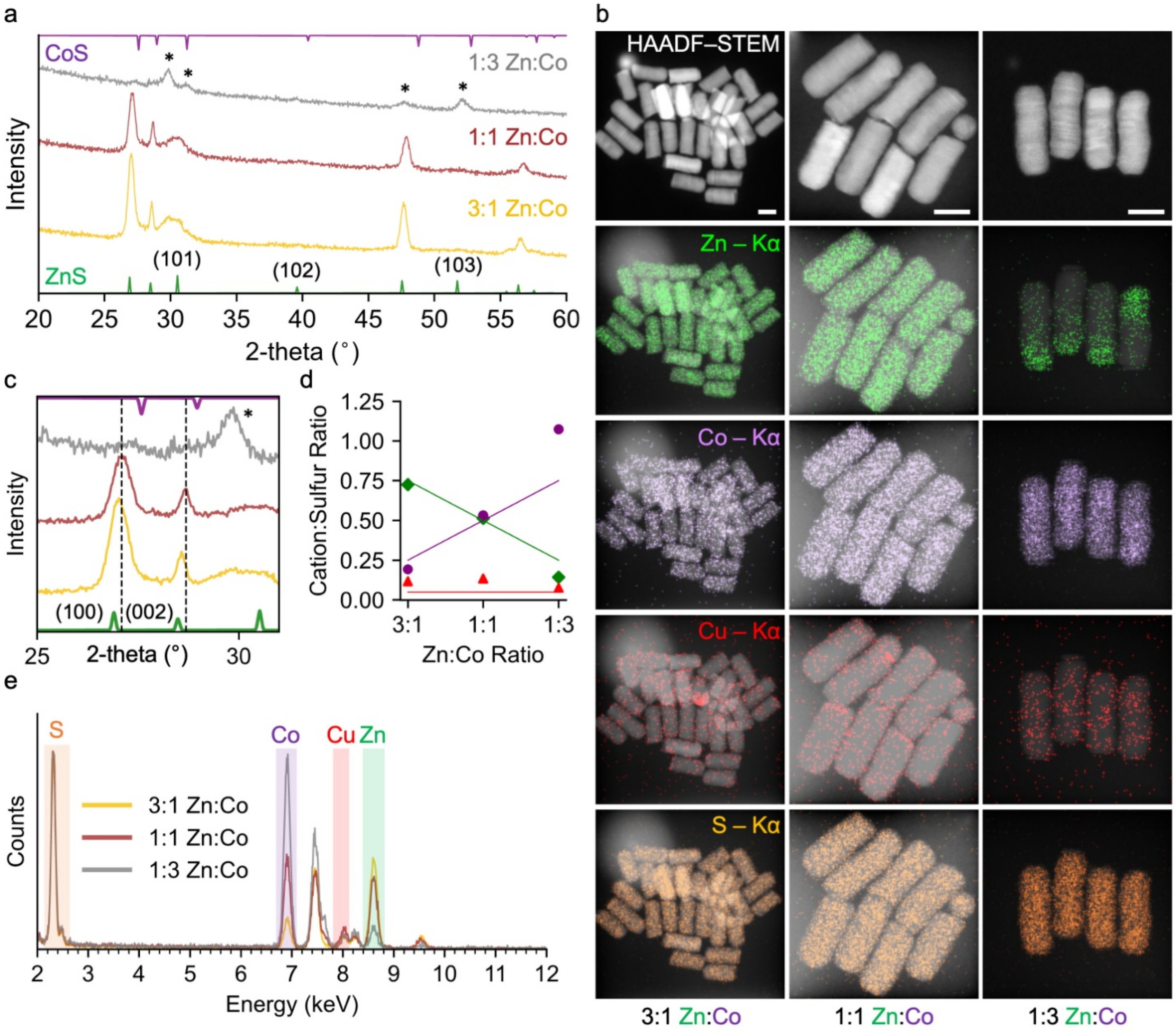

Figure 6. (a) Powder XRD patterns for the 3:1, 1:1, and 1:3 (bottom to top) Zn:Co simultaneous cation exchange reaction on $Cu_{1.8}S$ rods (x = 0.75 is grey, x = 0.5 is brown, and x = 0.25 is yellow). Reference XRD patterns for wurtzite ZnS[53] (green) and wurtzite CoS[54] (purple) are shown for comparison. Asterisks (*) correspond to reflections due to Co_9S_8.[56] (b) HAADF-STEM images and STEM-EDS element maps for Zn, Co, Cu, and S (shown overlaid on the HAADF-STEM images) for all three Zn:Co compositions: 3:1 Zn:Co (left), 1:1 Zn:Co (middle), and 1:3 Zn:Co (right). All scale bars are 20 nm. An enlarged region of the XRD pattern in (a) is shown in (c) from 25 – 30°, highlighting the (100) and (002) peaks. (d) Plot of cation to sulfur ratios (from the EDS spectra) for all three Zn:Co compositions. (Zn:S = green diamonds, Co:S =

purple spheres, Cu:S = red triangles.) For the Zn:S and Co:S values, the lines show the expected cation:sulfur ratios based on the $ZnCl_2$:$CoCl_2$ loadings. For the Cu:S value, the line is fixed at 5%, which is considered to be the approximate residual amount of copper after exchange. (e) EDS spectra for all three compositions (on Ni TEM grids), normalized to sulfur.

Additional analysis of the XRD data across all samples provides deeper insights into the nature of the solid solution. For the nanorods, the (10*l*) peaks for all three solid solution compositions are broad, with increasing broadness as the Co content in the solid solution increases (Figure 6a). A similar phenomenon exists for the nanosphere products, with the intensity of the same (10*l*) peaks decreasing with increasing Co content (Figure 2a). Wurtzite ZnS nanorods made through cation exchange form a high density of stacking faults, which interrupt the hcp anion stacking with regions of ccp. Because the $Cu_{1.8}S$ templates adopt a distorted hcp structure, converting hcp to ccp requires lateral shifting of the close packed planes. Analogous shifting is required to transform hcp $Cu_{1.8}S$ to ccp Co_9S_8. Importantly, the presence of these stacking faults leads to a decrease in the intensity of the (10*l*) peaks.[60] For both nanorods that fully converted to $Co_xZn_{1-x}S$ solid solutions stacking faults are observed in the HAADF-STEM (Figure 6b) images. This observation shows the $Co_xZn_{1-x}S$ solid solution retains features expected in cation exchange synthesized ZnS nanorods.[60]

Optical Properties of $Co_xZn_{1-x}S$ *vs. ZnS–CoS*

Figure 7a shows a picture of vials containing spherical nanoparticles (suspended in toluene) of the zinc sulfide and cobalt sulfide end members, as well as the 3:1, 1:1, and 1:3 Zn:Co solid solutions. As expected, all nanoparticle suspensions are optically transparent, given their size and colloidal dispersibility, and the zinc sulfide sample is colorless while the cobalt sulfide sample is black. We use Co_xS to refer to cobalt sulfide that is present as a mixture of wurtzite CoS and pentlandite Co_9S_8; this mixture is well documented in Co^{2+} exchange reactions of copper sulfide nanoparticles.[16,17] Both the zinc sulfide and cobalt sulfide nanospheres were synthesized by cation exchange of the same copper sulfide template used to make the solid solutions (Figure S13). For the $Co_xZn_{1-x}S$ solid solution nanoparticles, the 3:1 Zn:Co product is yellow, the 1:1 Zn:Co product is brown, and the 1:3 Zn:Co product is black (Figure 7a). The other morphologies exhibit similar colors but are more opaque due to the larger particle sizes and their tendency to aggregate along their long or flat dimensions; we therefore focus on the spherical nanoparticles. These colored solid solutions are accessible because the exchange of both cations is occurring simultaneously to generate a solid solution (Figure 7a).

Each of the solid solution samples shown were characterized by UV-Vis-NIR absorption spectroscopy. Wurtzite ZnS is a well-known semiconductor,[63] and the absorption spectrum for this end member (Figure 7a, green) shows a sharp absorbance near 335 nm corresponding to the excitation of an electron across its band gap, as expected.[63,64] Co_9S_8 is known to be metallic and CoS is likely metallic, and therefore as expected, the spherical cobalt sulfide end member exhibits relatively constant absorbance in the visible region (Figure 7a, purple). The 3:1 Zn:Co solid solution, which is yellow in the picture in Figure 7a, also appears to be semiconducting like ZnS, having a relatively sharp absorbance starting around 500 nm. Compared to ZnS, the absorbance feature that corresponds to the band gap is significantly broadened and shifted to higher wavelengths. The 1:1 Zn:Co solid solution, which appears brown in the picture in Figure 7a, is also semiconducting, but with an even broader absorbance feature than the 3:1 Zn:Co solid solution. The broadening of the band gap has been observed in Co-doped ZnS nanoparticles, where an increase in the amount of Co^{2+} incorporated into ZnS nanoparticles resulted in a transition from a direct to an indirect band gap.[64] In both products, there is also an absorbance feature near 730–750 nm, which corresponds to a transition from the $^4A_2$ (F) to $^4T_1$ (P) bands due to Co^{2+} occupying tetrahedral sites in Co-doped ZnS.[39,64–66] Both the 3:1 and 1:1 solid solutions are therefore semiconducting with band gaps broadened and shifted to lower energies with increasing Co^{2+} content. However, in the 1:3 Zn:Co solid solution, there is no absorbance feature near 732 nm and absorbance is nearly flat across the entire visible region, indicating metallic character that is more analogous to that of the cobalt sulfide end member. This indicates that within the $Co_xZn_{1-x}S$ solid solution, there is a transition from semiconducting to metallic behavior.

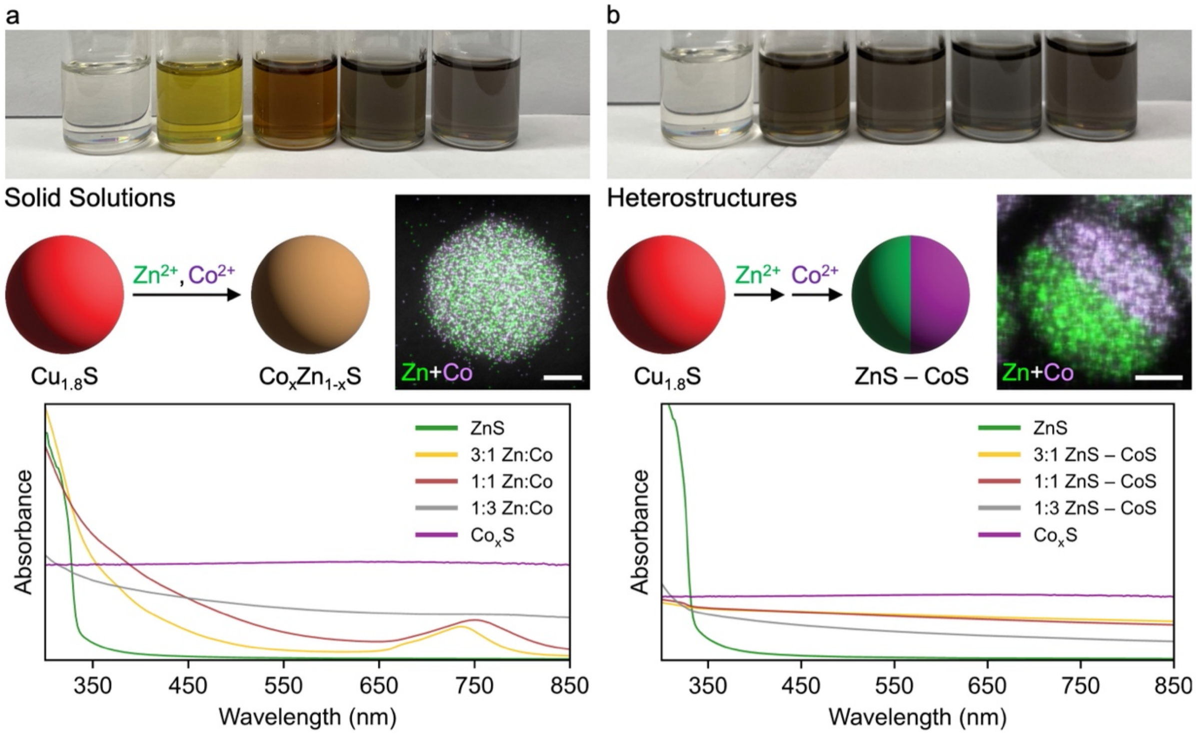

Figure 7. (a) Photographs of vials containing (from left to right) ZnS, $Co_{0.20}Zn_{0.75}S$, $Co_{0.43}Zn_{0.50}S$, $Co_{0.72}Zn_{0.27}S$, and Co_xS spherical nanoparticles, made by simultaneous exchange of Zn^{2+} and Co^{2+} cations as shown by the cartoon, suspended in toluene. The solid solution nanoparticles range from yellow to brown to black, while the ZnS and Co_xS end members are colorless and black, respectively. A STEM-EDS element map of showing Zn and Co signals overlaid on a HAADF-STEM image for the $Co_{0.43}Zn_{0.50}S$ sample is also shown. (b) Photographs of vials containing ZnS (left), Co_xS (right), and CoS–ZnS heterostructures containing (from left of middle to right of middle) 25% CoS and 75% ZnS, 50% CoS and 50% ZnS, and 75% CoS and 25% ZnS, suspended in toluene. The heterostructured nanoparticles, which are made by sequential exchange of Zn^{2+} and Co^{2+} cations as shown by the cartoon, are all black. A STEM-EDS element map of showing Zn and Co signals overlaid on a HAADF-STEM image for a heterostructured nanoparticle containing 50% CoS and 50% ZnS is also shown. UV-Visible absorbance spectra are also shown for all samples in both (a) and (b). All scale bars are 5 nm.

The emergence of a composition-tunable band gap in all but the most Co-rich $Co_xZn_{1-x}S$ sample generated through *simultaneous* cation exchange is in sharp contrast to the largely additive optical properties that are present in compositionally-analogous CoS–ZnS heterostructures generated through *sequential* cation exchange (Figure 7b). For comparison with the solid solutions, ZnS–CoS heterostructured nanoparticles mirroring the compositions and morphologies of the $Co_xZn_{1-x}S$ solid solution nanoparticles were synthesized. Spherical $Cu_{1.8}S$ nanoparticles suspended in TOP were injected into a flask at 100 °C under Ar with different amounts of $ZnCl_2$ solutions followed by injection of excess amounts of $CoCl_2$ solutions, ultimately producing spherical heterostructured ZnS–CoS nanoparticles with average compositions of 75% ZnS with 25% CoS, 50% ZnS with 50% CoS, and 25% ZnS with 75% CoS. STEM-EDS element maps of these heterostructured nanoparticles show that the Zn and Co signals are segregated on opposite sides and the relative proportions of each metal sulfide in each type of particle tracks well with the amount of $ZnCl_2$ used during the first exchange step (Figure S14). XRD data also support the presence of both CoS and ZnS in the heterostructured particles (Figure S14).

Heterostructured nanoparticles often have properties that represent a sum of the properties exhibited by the individual materials that comprise them, in addition to any synergistic interactions across the interface. The pictures of colloidal suspensions of the ZnS–CoS heterostructured nanoparticles in Figure 7b indeed contrast with those of the compositionally-analogous $Co_xZn_{1-x}S$ solid solutions, as all of the heterostructured nanoparticles appear black since they combine a metallic material (cobalt sulfide) that is black and a wide band gap semiconductor (zinc sulfide) that is transparent in the visible. The corresponding UV-Vis spectra are consistent, with the heterostructured nanoparticles having relatively flat absorbance through the visible region (analogous to cobalt sulfide), along with an absorption onset near 335 nm corresponding to ZnS (Figure 7b). By carrying out the cation exchange reaction *simultaneously* instead of *sequentially*, the solid solution $Co_xZn_{1-x}S$ is formed instead of a ZnS–CoS heterostructure, and these two variants have fundamentally different physical properties, as reflected by their different UV-Vis absorption spectra.

Heterostructured nanoparticles containing $Co_xZn_{1-x}S$

We now know that the ratio of total cations to copper sulfide is the critical factor for forming solid solutions through simultaneous multi-cation exchange. We also now know that morphology has little impact on the formation of the semiconducting $Co_xZn_{1-x}S$ solid solution in this system and that different spectral features are observed in compositionally related solid solutions versus heterostructures. We therefore sought to design, synthesize, and characterize a series of nanoparticles that progressively evolve from the template $Cu_{1.8}S$ rods to a heterostructured $Co_xZn_{1-x}S$–$Cu_{1.8}S$ rod to a heterostructured $Co_xZn_{1-x}S$–ZnS rod (Figure 8a). $Co_xZn_{1-x}S$–$Cu_{1.8}S$ rods were targeted using partial simultaneous Zn^{2+}/Co^{2+} exchange, which substoichiometrically limited the total amount of cations available for exchange. Here, a suspension of $Cu_{1.8}S$ nanorods (Figure 8b) in TOP was injected into a flask at 100 °C under Ar containing a solution having a 1:1 ratio of $ZnCl_2$:$CoCl_2$ but with the molar ratio of total cations (Zn^{2+} and Co^{2+}) to copper sulfide equaling 0.5, instead of 1.1, which was used previously. STEM-EDS element maps (Figure 8c and S15a-d) show that the resulting nanorods are composed of both $Co_xZn_{1-x}S$ and $Cu_{1.8}S$. The regions corresponding to $Co_xZn_{1-x}S$ have high contrast stacking faults, as seen in the HAADF images (Figures S15a-d), as expected based on previous exchanges on the nanorods, as well as literature for the end-member systems[60]. The formation of the $Co_xZn_{1-x}S$ domain indicates that even with unreacted $Cu_{1.8}S$, the metastable solid solution forms instead of the end members. The $Co_xZn_{1-x}S$–ZnS heterostructures were made following the same procedure to synthesize $Co_xZn_{1-x}S$–$Cu_{1.8}S$ followed by an injection of excess Zn^{2+} solution to exchange the remaining $Cu_{1.8}S$ region with Zn^{2+} to form ZnS (Figure 8d) (Figure S15e-f). It is worth noting that the Co^{2+} in the $Co_xZn_{1-x}S$ regions remains in those regions and does not diffuse into the newly formed ZnS region. This provides additional evidence that formation of the $Co_xZn_{1-x}S$ solid solution requires simultaneous Co^{2+}/Zn^{2+} exchange.

UV-Vis-NIR spectra of the three products ($Cu_{1.8}S$, $Co_{0.5}Zn_{0.5}S$–$Cu_{1.8}S$, $Co_{0.5}Zn_{0.5}S$–ZnS) are shown Figure 8e. The $Cu_{1.8}S$ nanorods have absorbance features in the range of 1200-1500 nm, due to its plasmon band, as well as starting around 800 nm, due to its band gap. The heterostructured $Co_{0.5}Zn_{0.5}S$–$Cu_{1.8}S$ nanorods combine the features of $Cu_{1.8}S$ (plasmon band and band gap) with those of the $Co_xZn_{1-x}S$ solid solution, which include absorption features due to tetrahedrally coordinated Co^{2+} around 732 nm and the band gap that absorbs starting near 650 nm. Transformation into $Co_{0.5}Zn_{0.5}S$–ZnS eliminates the plasmonic feature but retains the absorbance around 732 nm and the broad bandgap absorbance while adding the sharp absorption onset near 350 nm for ZnS. Despite all three of these materials being nominally brown, they have distinct optical absorption features based on their compositions and composition distributions.

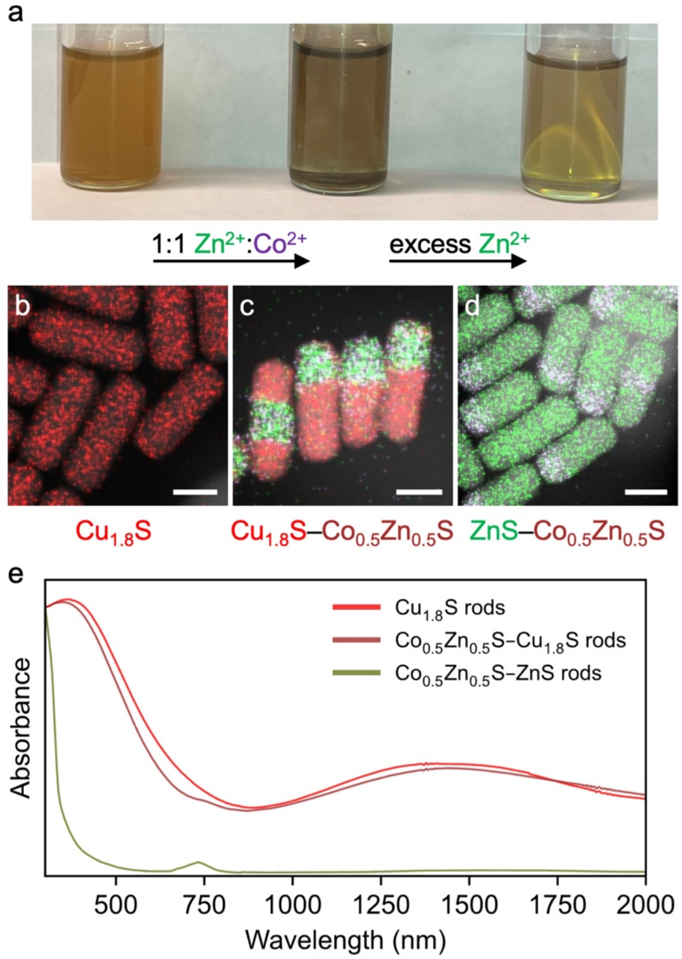

Figure 8. (a) Photograph of vials containing (left to right) $Cu_{1.8}S$, $Cu_{1.8}S$–$Co_{0.5}Zn_{0.5}S$, and ZnS–$Co_{0.5}Zn_{0.5}S$ nanorods suspended in toluene. STEM-EDS element maps (Cu = red, Zn = green, Co = purple, overlaid on HAADF-STEM images) are shown for (b) $Cu_{1.8}S$ nanorods, (c) $Cu_{1.8}S$–$Co_{0.5}Zn_{0.5}S$ heterostructured nanorods, and (d) ZnS–$Co_{0.5}Zn_{0.5}S$ heterostructured nanorods. (e) UV-Vis NIR absorbance spectra of $Cu_{1.8}S$, $Cu_{1.8}S$–$Co_{0.5}Zn_{0.5}S$, and ZnS–$Co_{0.5}Zn_{0.5}S$ nanorods. All scale bars are 20 nm.

CONCLUSIONS

Nanoparticle spheres, rods, and plates that span the metastable wurtzite $Co_xZn_{1-x}S$ solid solution, as verified by first-principles predictions of convex hulls for derivative structures, were synthesized through a simultaneous multi-cation exchange reaction. For the spherical nanoparticles, the composition could be tuned simply by changing the ratio of the $ZnCl_2$ and $CoCl_2$ reagents used for the exchange, as long as the ratio of total incoming metal cations to copper sulfide remained close to 1:1. When a significant excess was used, the reactivity of Co^{2+} outcompeted that of Zn^{2+}, leading to cobalt sulfide (*i.e.*, end member) byproducts The plates and rods behaved similarly to the spheres, although they did not form solid solutions at higher Co^{2+} concentrations because their anisotropic morphologies enhanced the difference in reactivity between Co^{2+} and Zn^{2+}, leading to the formation of cobalt sulfides. Composition-dependent optical properties were observed for $Co_xZn_{1-x}S$, with a color change and transformation from semiconducting (x = 0.25, 0.50) to metallic ($x = 0.75$) behavior. The optical properties of $Co_xZn_{1-x}S$ were distinct from those of phase-segregated CoS–ZnS, and this observation led to the design and synthesis of various heterostructured nanoparticles that combined the $Co_xZn_{1-x}S$ solid solution with other materials, including $Cu_{1.8}S$ and ZnS.

The key to balancing reactivity is to carry out the multi-cation exchange reactions using a low molar ratio of total cations to copper sulfide. Under this condition, the cation composition of the exchange solution matches that in the exchanged nanoparticles, as both cations can co-exchange simultaneously. An increase in this ratio, where both cations are available in significant excess, opens up competition between the two cations, with one (Co^{2+}) over-exchanging and leading to the formation of end-member byproducts. On the other hand, choosing ratios of total cations to copper sulfide that are less than stoichiometric limits the extent of exchange, enabling the formation of $Co_xZn_{1-x}S$–$Cu_{1.8}S$ heterostructured nanoparticles, which can further be transformed into $Co_xZn_{1-x}S$–ZnS following a subsequent Zn^{2+} exchange. These observations reveal how both order of addition (sequential vs. simultaneous) and reactivity influences homogeneous vs heterogeneous incorporation of multiple metal cations in products after exchange. These products also demonstrate how the composition and composition distribution influences the optical properties of the nanoparticle materials.

The formation of solid solutions can be challenging in nanoparticle synthesis, as it requires balancing the reactivities of multiple cations along with other reagents and components of reactions, including reducing agents, counterions, surfactants/ligands, solvents, precursor concentrations, temperatures, reaction times, and, most importantly, the complex interplay among all of these factors. Cation exchange presents itself as a simplified platform to design solid solution nanoparticles where the key chemical challenges are balancing cation reactivity relative to a template material and where composition can be easily tuned by changing the ratio of cations. This simplification in experimental design to generate solid solutions expands our ability to target and synthesize high quality nanoparticles having complex and tunable compositions.

ASSOCIATED CONTENT

SUPPORTING INFORMATION

Additional experimental details, XRD, TEM, STEM-EDS, and UV-Vis-NIR data, as well as sample metastable configurations of $Co_xZn_{1-x}S$. This material is available free of charge via the Internet at http://pubs.acs.org.

AUTHOR INFORMATION

Corresponding Authors

Raymond E. Schaak – *Department of Chemistry*, *Department of Chemical Engineering*, and *Materials Research Institute*, *The Pennsylvania State University, University Park, Pennsylvania 16802, United States*; Email: res20@psu.edu

Ismaila Dabo – *Department of Materials Science and Engineering* and *Materials Research Institute*, *The Pennsylvania State University, University Park, Pennsylvania 16802, United States*; Email: ixd4@psu.edu

Authors

Connor R. McCormick – *Department of Chemistry*, *The Pennsylvania State University, University Park, Pennsylvania 16802, United States*

Steven M. Baksa – *Department of Materials Science and Engineering*, *The Pennsylvania State University, University Park, Pennsylvania 16802, United States*

Joseph M. Veglak – *Department of Chemistry*, *The Pennsylvania State University, University Park, Pennsylvania 16802, United States*

Notes

The authors declare no competing financial interest.

ACKNOWLEDGMENT

With the exceptions listed below, this work was supported by the U.S. National Science Foundation under grant DMR-2210442. TEM imaging, X-ray diffraction, and UV-vis-NIR spectroscopy were performed at the Materials Characterization Lab of the Penn State Materials Research Institute. The first-principles simulations were supported by the U.S. Department of Energy, Office of Science, Office of Basic Energy Sciences Energy Frontier Research Centers program under Award Number DE-SC0021118 (Center for 3D Ferroelectric Microelectronics). First-principles calculations and convex-hull analyses were conducted using the Penn State ROAR supercomputer.

REFERENCES

(1) Flanagan, J. C.; Keating, L. P.; Kalasad, M. N.; Shim, M. Extending the Spectral Range of Double-Heterojunction Nanorods by Cation Exchange-Induced Alloying. *Chem. Mater.* **2019**, *31*, 9307–9316.

(2) Tang, Y.; Yang, H.; Sun, J.; Xia, M.; Guo, W.; Yu, L.; Yan, J.; Zheng, J.; Chang, L.; Gao, F. Phase-Pure Pentlandite $Ni_{4.3}Co_{4.7}S_8$ Binary Sulfide as an Efficient Bifunctional Electrocatalyst for Oxygen Evolution and Hydrogen Evolution. *Nanoscale* **2018**, *10*, 10459–10466.

(3) M Giebultowicz, S. T.; Klosowski, P.; Rhyne, J. J.; Udovic, T. J.; Furdyna, J. K.; Giriat, W. Magnetic Exchange Interactions in Co-Based II-VI Diluted Magnetic Semiconductors. *Phys. Rev. B* **1990**, *41*, 504–513.

(4) Yang, J.; Zhang, Y.; Sun, C.; Guo, G.; Sun, W.; Huang, W.; Yan, Q.; Dong, X. Controlled Synthesis of Zinc Cobalt Sulfide Nanostructures in Oil Phase and Their Potential Applications in Electrochemical Energy Storage. *J. Mater. Chem. A* **2015**, *3*, 11462–11470.

(5) Regulacio, M. D.; Han, M. Y. Composition-Tunable Alloyed Semiconductor Nanocrystals. *Acc. Chem. Res.* **2010**, *43*, 621–630.

(6) Prusty, D.; Paramanik, L.; Parida, K. Recent Advances on Alloyed Quantum Dots for Photocatalytic Hydrogen Evolution: A Mini-Review. *Energy Fuels* **2021**, *35*, 4670–4686.

(7) Li, Q.; Meng, H.; Zhou, P.; Zheng, Y.; Wang, J.; Yu, J.; Gong, J. $Zn_{1-x}Cd_xS$ Solid Solutions with Controlled Bandgap and Enhanced Visible-Light Photocatalytic H_2-Production Activity. *ACS Catal.* **2013**, *3*, 882–889.

(8) Wang, Y. H. A.; Zhang, X.; Bao, N.; Lin, B.; Gupta, A. Synthesis of Shape-Controlled Monodisperse Wurtzite $CuIn_xGa_{1-x}S_2$ Semiconductor Nanocrystals with Tunable Band Gap. *J. Am. Chem. Soc.* **2011**, *133*, 11072–11075.

(9) Yarema, O.; Yarema, M.; Wood, V. Tuning the Composition of Multicomponent Semiconductor Nanocrystals: The Case of I-III-VI Materials. *Chem. Mater*. **2018**, *30*, 1446–1461.

(10) Williamson, E. M.; Tappan, B. A.; Mora-Tamez, L.; Barim, G.; Brutchey, R. L. Statistical Multiobjective Optimization of Thiospinel $CoNi_2S_4$ Nanocrystal Synthesis via Design of Experiments. *ACS Nano* **2021**, *15*, 9422–9433.

(11) Beberwyck, B. J.; Surendranath, Y.; Alivisatos, A. P. Cation Exchange: A Versatile Tool for Nanomaterials Synthesis. *J. Phys. Chem. C* **2013**, *117*, 19759–19770.

(12) de Trizio, L.; Manna, L. Forging Colloidal Nanostructures via Cation Exchange Reactions. *Chem. Rev.* **2016**, *116*, 10852–10887.

(13) Fenton, J. L.; Steimle, B. C.; Schaak, R. E. Structure-Selective Synthesis of Wurtzite and Zincblende ZnS, CdS, and $CuInS_2$ Using Nanoparticle Cation Exchange Reactions. *Inorg. Chem.* **2019**, *58*, 672–678.

(14) Zhai, Y.; Flanagan, J. C.; Shim, M. Lattice Strain and Ligand Effects on the Formation of $Cu_{2-x}S$/I-III-VI_2 Nanorod Heterostructures through Partial Cation Exchange. *Chem. Mater.* **2017**, *29*, 6161–6167.

(15) Hinterding, S. O. M.; Berends, A. C.; Kurttepeli, M.; Moret, M. E.; Meeldijk, J. D.; Bals, S.; van der Stam, W.; de Mello Donega, C. Tailoring Cu^+ for Ga^{3+} Cation Exchange in $Cu_{2-x}S$ and $CuInS_2$ Nanocrystals by Controlling the Ga Precursor Chemistry. *ACS Nano* **2019**, *13*, 12880–12893.

(16) Butterfield, A. G.; McCormick, C. R.; Veglak, J. M.; Schaak, R. E. Morphology-Dependent Phase Selectivity of Cobalt Sulfide during Nanoparticle Cation Exchange Reactions. *J. Am. Chem. Soc.* **2021**, *143*, 7915–7919.

(17) Li, Z.; Saruyama, M.; Asaka, T.; Tatetsu, Y.; Teranishi, T. Determinants of Crystal Structure Transformation of Ionic Nanocrystals in Cation Exchange Reactions. *Science* **2021**, *373*, 332–337.

(18) Fenton, J. L.; Steimle, B. C.; Schaak, R. E. Tunable Intraparticle Frameworks for Creating Complex Heterostructured Nanoparticle Libraries. *Science* **2018**, *360*, 513–517.

(19) Sharp, C. G.; Leach, A. D. P.; Macdonald, J. E. Tolman's Electronic Parameter of the Ligand Predicts Phase in the Cation Exchange to $CuFeS_2$ Nanoparticles. *Nano Lett.* **2020**, *20*, 8556–8562.

(20) Lesnyak, V.; Brescia, R.; Messina, G. C.; Manna, L. Cu Vacancies Boost Cation Exchange Reactions in Copper Selenide Nanocrystals. *J. Am. Chem. Soc.* **2015**, *137*, 9315–9323.

(21) Li, H.; Zanella, M.; Genovese, A.; Povia, M.; Falqui, A.; Giannini, C.; Manna, L. Sequential Cation Exchange in Nanocrystals: Preservation of Crystal Phase and Formation of Metastable Phases. *Nano Lett.* **2011**, *11*, 4964–4970.

(22) Fenton, J. L.; Schaak, R. E. Structure-Selective Cation Exchange in the Synthesis of Zincblende MnS and CoS Nanocrystals. *Angew. Chem., Int. Ed.* **2017**, *56*, 6464–6467.

(23) Zhai, Y.; Shim, M. Effects of Copper Precursor Reactivity on the Shape and Phase of Copper Sulfide Nanocrystals. *Chem. Mater.* **2017**, *29*, 2390–2397.

(24) McCormick, C. R.; Schaak, R. E. Simultaneous Multication Exchange Pathway to High-Entropy Metal Sulfide Nanoparticles. *J. Am. Chem. Soc.* **2021**, *143*, 1017–1023.

(25) Van Der Stam, W.; Berends, A. C.; Rabouw, F. T.; Willhammar, T.; Ke, X.; Meeldijk, J. D.; Bals, S.; De Mello Donega, C. Luminescent $CuInS_2$ Quantum Dots by Partial Cation Exchange in $Cu_{2-x}S$ Nanocrystals. *Chem. Mater.* **2015**, *27*, 621–628.

(26) De Trizio, L.; Prato, M.; Genovese, A.; Casu, A.; Povia, M.; Simonutti, R.; Alcocer, M. J. P.; D'Andrea, C.; Tassone, F.; Manna, L. Strongly Fluorescent Quaternary Cu-In-Zn-S Nanocrystals Prepared from $Cu_{1-x}InS_2$ Nanocrystals by Partial Cation Exchange. *Chem. Mater.* **2012**, *24*, 2400–2406.

(27) Akkerman, Q. A.; Genovese, A.; George, C.; Prato, M.; Moreels, I.; Casu, A.; Marras, S.; Curcio, A.; Scarpellini, A.; Pellegrino, T.; Manna, L.; Lesnyak, V. From Binary Cu_2S to Ternary Cu-In-S and Quaternary Cu-In-Zn-S Nanocrystals with Tunable Composition via Partial Cation Exchange. *ACS Nano* **2015**, *9*, 521–531.

(28) De Trizio, L.; Li, H.; Casu, A.; Genovese, A.; Sathya, A.; Messina, G. C.; Manna, L. Sn Cation Valency Dependence in Cation Exchange Reactions Involving $Cu_{2-x}Se$ Nanocrystals. *J. Am. Chem. Soc.* **2014**, *136*, 16277–16284.

(29) Liu, Y.; Liu, M.; Yin, D.; Wei, W.; Prasad, P. N.; Swihart, M. T. Kuramite Cu_3SnS_4 and Mohite Cu_2SnS_3 Nanoplatelet Synthesis Using Covellite CuS Templates with Sn(II) and Sn(IV) Sources. *Chem. Mater.* **2017**, *29*, 3555–3562.

(30) Lesnyak, V.; George, C.; Genovese, A.; Prato, M.; Casu, A.; Ayyappan, S.; Scarpellini, A.; Manna, L. Alloyed Copper Chalcogenide Nanoplatelets via Partial Cation Exchange Reactions. *ACS Nano* **2014**, *8*, 8407–8418.

(31) Lee, S.; Yoon, D. E.; Kim, D.; Shin, D. J.; Jeong, B. G.; Lee, D.; Lim, J.; Bae, W. K.; Lim, H. K.; Lee, D. C. Direct Cation Exchange of CdSe Nanocrystals into ZnSe Enabled by Controlled Binding between Guest Cations and Organic Ligands. *Nanoscale* **2019**, *11*, 15072–15082.

(32) Steimle, B. C.; Fenton, J. L.; Schaak, R. E. Rational Construction of a Scalable Heterostructured Nanorod Megalibrary. *Science* **2020**, *367*, 418–424.

(33) Fenton, J. L.; Steimle, B. C.; Schaak, R. E. Exploiting Crystallographic Regioselectivity to Engineer Asymmetric Three-Component Colloidal Nanoparticle Isomers Using Partial Cation Exchange Reactions. *J. Am. Chem. Soc.* **2018**, *140*, 6771–6775.

(34) McCormick, C. R.; Katzbaer, R. R.; Steimle, B. C.; Schaak, R. E. Combinatorial Cation Exchange for the Discovery and Rational Synthesis of Heterostructured Nanorods. *Nat. Synth.* **2023**, *2*, 152–161.

(35) Tong, H.; Bai, W.; Yue, S.; Gao, Z.; Lu, L.; Shen, L.; Dong, S.; Zhu, J.; He, J.; Zhang, X. Zinc Cobalt Sulfide Nanosheets Grown on Nitrogen-Doped Graphene/Carbon Nanotube Film as a High-Performance Electrode for Supercapacitors. *J. Mater. Chem. A* **2016**, *4*, 11256–11263.

(36) Gao, X.; Chang, Q.; Hong, J.; Long, D.; Jin, G.; Xiao, X. Zinc Cobalt Sulfide Microspheres as a High-Performance Electrode Material for Supercapacitors. *ChemistrySelect* **2018**, *3*, 13751–13758.

(37) Li, H.; Li, Z.; Sun, M.; Wu, Z.; Shen, W.; Fu, Y. Q. Zinc Cobalt Sulfide Nanoparticles as High Performance Electrode Material for Asymmetric Supercapacitor. *Electrochim. Acta* **2019**, *319*, 716–726.

(38) Yu, K.; Wang, J.; Wang, X.; Li, Y.; Liang, C. Zinc–Cobalt Bimetallic Sulfide Anchored on the Surface of Reduced Graphene Oxide Used as Anode for Lithium Ion Battery. *J. Solid State Chem.* **2020**, *290*, 121619.

(39) Patel, K.; Deshpande, M. P.; Chaki, S. H. Effect of Cobalt Doping on ZnS Nanoparticles Synthesized by Microwave Irradiation. *J. Mater. Sci.: Mater Electron* **2017**, *28*, 5029–5036.

(40) Steimle, B. C.; Fagan, A. M.; Butterfield, A. G.; Lord, R. W.; McCormick, C. R.; Di Domizio, G. A.; Schaak, R. E. Experimental Insights into Partial Cation Exchange Reactions for Synthesizing Heterostructured Metal Sulfide Nanocrystals. *Chem. Mater.* **2020**, *32*, 5461–5482.

(41) Perdew, J. P.; Burke, K.; Ernzerhof, M. Generalized Gradient Approximation Made Simple. *Phys. Rev. Lett.* **1996**, *77*, 3865–3868.

(42) van Setten, M. J.; Giantomassi, M.; Bousquet, E.; Verstraete, M. J.; Hamann, D. R.; Gonze, X.; Rignanese, G.-M. The PseudoDojo: Training and Grading a 85 Element Optimized Norm-Conserving Pseudopotential Table. *Comput. Phys. Commun.* **2017**, *226*, 39-54.

(43) Lejaeghere, K.; Bihlmayer, G.; Björkman, T.; Blaha, P.; Blügel, S.; Blum, V.; Caliste, D.; Castelli, I. E.; Clark, S. J.; Dal Corso, A.; De Gironcoli, S.; Deutsch, T.; Dewhurst, J. K.; Di Marco, I.; Draxl, C.; Dułak, M.; Eriksson, O.; Flores-Livas, J. A.; Garrity, K. F.; Genovese, L.; Giannozzi, P.; Giantomassi, M.; Goedecker, S.; Gonze, X.; Grånäs, O.; Gross, E. K. U.; Gulans, A.; Gygi, F.; Hamann, D. R.; Hasnip, P. J.; Holzwarth, N. A. W.; Iuşan, D.; Jochym, D. B.; Jollet, F.; Jones, D.; Kresse, G.; Koepernik, K.; Küçükbenli, E.; Kvashnin, Y. O.; Locht, I. L. M.; Lubeck, S.; Marsman, M.; Marzari, N.; Nitzsche, U.; Nordström, L.; Ozaki, T.;

Paulatto, L.; Pickard, C. J.; Poelmans, W.; Probert, M. I. J.; Refson, K.; Richter, M.; Rignanese, G. M.; Saha, S.; Scheffler, M.; Schlipf, M.; Schwarz, K.; Sharma, S.; Tavazza, F.; Thunström, P.; Tkatchenko, A.; Torrent, M.; Vanderbilt, D.; Van Setten, M. J.; Van Speybroeck, V.; Wills, J. M.; Yates, J. R.; Zhang, G. X.; Cottenier, S. Reproducibility in Density Functional Theory Calculations of Solids. *Science* **2016**, *351*, aad3000.

(44) Hamann, D. R. Optimized Norm-Conserving Vanderbilt Pseudopotentials. *Phys. Rev. B: Condens. Matter Mater. Phys.* **2013**, *88*, 85117.

(45) Giannozzi, P.; Baroni, S.; Bonini, N.; Calandra, M.; Car, R.; Cavazzoni, C.; Ceresoli, D.; Chiarotti, G. L.; Cococcioni, M.; Dabo, I.; Dal Corso, A.; De Gironcoli, S.; Fabris, S.; Fratesi, G.; Gebauer, R.; Gerstmann, U.; Gougoussis, C.; Kokalj, A.; Lazzeri, M.; Martin-Samos, L.; Marzari, N.; Mauri, F.; Mazzarello, R.; Paolini, S.; Pasquarello, A.; Paulatto, L.; Sbraccia, C.; Scandolo, S.; Sclauzero, G.; Seitsonen, A. P.; Smogunov, A.; Umari, P.; Wentzcovitch, R. M. QUANTUM ESPRESSO: A Modular and Open-Source Software Project for Quantum Simulations of Materials. *J. Phys.: Condens. Matter* **2009**, *21*, 395502.

(46) Giannozzi, P.; Andreussi, O.; Brumme, T.; Bunau, O.; Buongiorno Nardelli, M.; Calandra, M.; Car, R.; Cavazzoni, C.; Ceresoli, D.; Cococcioni, M.; Colonna, N.; Carnimeo, I.; Dal Corso, A.; De Gironcoli, S.; Delugas, P.; Distasio, R. A.; Ferretti, A.; Floris, A.; Fratesi, G.; Fugallo, G.; Gebauer, R.; Gerstmann, U.; Giustino, F.; Gorni, T.; Jia, J.; Kawamura, M.; Ko, H. Y.; Kokalj, A.; Kücükbenli, E.; Lazzeri, M.; Marsili, M.; Marzari, N.; Mauri, F.; Nguyen, N. L.; Nguyen, H. V.; Otero-De-La-Roza, A.; Paulatto, L.; Poncé, S.; Rocca, D.; Sabatini, R.; Santra, B.; Schlipf, M.; Seitsonen, A. P.; Smogunov, A.; Timrov, I.; Thonhauser, T.; Umari, P.; Vast, N.; Wu, X.; Baroni, S. Advanced Capabilities for Materials Modelling with Quantum ESPRESSO. *J. Phys.: Condens. Matter* **2017**, *29*, 465901.

(47) Perdew, J. P.; Chevary, J. A.; Vosko, S. H.; Jackson, K. A.; Pederson, M. R.; Singh, D. J.; Fiolhais, C. Atoms, Molecules, Solids, and Surfaces: Applications of the Generalized Gradient Approximation for Exchange and Correlation. *Phys. Rev. B* **1992**, *46* (11), 6671–6687.

(48) Becke, A. D. Density-Functional Exchange-Energy Approximation with Correct Asymptotic Behavior. *Phys. Rev. A* **1988**, *38*, 3098–3100.

(49) Langreth, D. C.; Mehl', M. J. Beyond the Local-Density Approximation in Calculations of Ground-State Electronic Properties. *Phys. Rev. B* **1983**, *28*, 1809–1834.

(50) Hart, G. L. W.; Forcade, R. W. Algorithm for Generating Derivative Structures. *Phys. Rev. B* **2008**, *77*, 224115.

(51) Hart, G. L. W.; Forcade, R. W. Generating Derivative Structures from Multilattices: Algorithm and Application to hcp alloys. *Phys. Rev. B* **2009**, *80*, 014120.

(52) Ångqvist, M.; Muñoz, W. A.; Rahm, J. M.; Fransson, E.; Durniak, C.; Rozyczko, P.; Rod, T. H.; Erhart, P. ICET – A Python Library for Constructing and Sampling Alloy Cluster Expansions. *Adv. Theory Simul.* **2019**, *2*, 1900015.

(53) Kisi, E. H.; Elcombe, M. M. *u* Parameters for the Wurtzite Structure of ZnS and ZnO Using Powder Neutron Diffraction. *Acta Cryst. C* **1989**, *45*, 1867–1870.

(54) Powell, A. E.; Hodges, J. M.; Schaak, R. E. Preserving Both Anion and Cation Sublattice Features during a Nanocrystal Cation-Exchange Reaction: Synthesis of Metastable Wurtzite-Type CoS and MnS. *J. Am. Chem. Soc.* **2016**, *138*, 471–474.

(55) Mumme, W. G.; Gable, R. W.; Petrícek, V. The Crystal Structure of Roxbyite, $Cu_{58}S_{32}$. *Can. Mineral.* **2012**, *50*, 423–430.

(56) Rajamani, V.; Prewitt, C. T. Refinement of the Structure of Co_9S_8. *Can Mineral* **1975**, *13*, 75–78.

(57) Evans, H. T. J. The Crystal Structures of Low Chalcocite and Djurleite. *Z Kristallogr.* **1979**, *150*, 299–320.

(58) Shannon, R. D.; Prewitt, C. T. Effective Ionic Radii in Oxides and Fluorides. *Acta Cryst. B* **1969**, *25*, 925–946.

(59) Becker, W.; Lutz, H. D. Phase Studies in the Systems CoS-MnS, CoS-ZnS, and CoS-CdS. *Mater. Res. Bull.* **1978**, *13*, 907–911.

(60) Butterfield, A. G.; Alameda, L. T.; Schaak, R. E. Emergence and Control of Stacking Fault Formation during Nanoparticle Cation Exchange Reactions. *J. Am. Chem. Soc.* **2021**, *143*, 1779–1783.

(61) Coughlan, C.; Ibáñez, M.; Dobrozhan, O.; Singh, A.; Cabot, A.; Ryan, K. M. Compound Copper Chalcogenide Nanocrystals. *Chem. Rev.* **2017**, *117*, 5865–6109.

(62) Young, H. L.; McCormick, C. R.; Butterfield, A. G.; Gomez, E. D.; Schaak, R. E. Postsynthetic Thiol-Induced Reshaping of Copper Sulfide Nanoparticles. *Chem. Mater.* **2022** *34*, 11014-11025.

(63) Fang, X.; Zhai, T.; Gautam, U. K.; Li, L.; Wu, L.; Bando, Y.; Golberg, D. ZnS Nanostructures: From Synthesis to Applications. *Prog. Mater. Sci.* **2011**, *56*, 175–287.

(64) Ren, G.; Lin, Z.; Wang, C.; Liu, W.; Zhang, J.; Huang, F.; Liang, J. Relationship between the Coprecipitation Mechanism, Doping Structure and Physical Properties of $Zn_{1-x}Co_xS$ Nanocrystallites. *Nanotechnology* **2007**, *18*, 35705.

(65) Martinez, U.; Lopez-Rivera, S. A.; Giriat, W.; Medina, F. Nature of the Absorption Bands in $Zn_{1-x}Co_xS$. *J. Cryst. Growth* **1994**, *138*, 913–916.

(66) Patel, S. P.; Pivin, J. C.; Chawla, A. K.; Chandra, R.; Kanjilal, D.; Kumar, L. Room Temperature Ferromagnetism in $Zn_{1-x}Co_xS$ Thin Films with Wurtzite Structure. *J. Magn. Magn. Mater.* **2011**, *323*, 2734–2740.

Table of Contents Graphic